

A phase-field model for DNA self-assembly

Marco Cappa,¹ Francesco Sciortino,¹ and Lorenzo Rovigatti¹

¹*Dipartimento di Fisica, Sapienza Università di Roma, P.le Aldo Moro 5, 00185 Rome, Italy*

We present a phase-field model based on the Cahn-Hilliard equation to investigate the kinetics of phase separation in DNA nanostar systems. Leveraging a realistic free-energy functional derived from Wertheim theory, our model captures the thermodynamic and dynamic properties of self-assembling DNA nanostars under various conditions. This approach allows for the study of both one-component and multi-component systems, including mixtures of different nanostar species and cross-linkers. Through numerical simulations, we demonstrate the model's ability to replicate experimental observations, including liquid-liquid phase separation, surface tension variation, and the structural organization of multi-component systems. Our results highlight the versatility and predictive power of the Cahn-Hilliard framework, particularly for complex systems where detailed simulations are computationally prohibitive. This work provides a robust foundation for studying DNA-based materials and their potential applications in nanotechnology and biophysics, including liquid-liquid phase separation in cellular environments.

I. INTRODUCTION

DNA constitutes a macromolecule of extraordinary interest from different points of view: its particular double helix conformation, combined with the hybridisation mechanism that allows the coupling between sequences of compatible nitrogenous bases [1], makes it an instrument of choice for the synthesis of innovative and versatile materials in the field of materials science, and a powerful means of investigation and experimentation at the biophysical level [2]; in this sense, significant are the uses that have been made of it (even in aggregate form) to create nanomachines [3], logical *gates* [4], nanostructures [5–8], to build vectors for *drug-delivery* [9] strategies, but also to investigate novel phenomena in soft matter systems [10–13]. In particular, the sequence-specific pairing mechanisms of DNA makes it particularly suitable to study phase separation processes, as they allow for a careful control on the bonding properties of the system [2, 11].

A class of DNA-based systems that has been used for this kind of investigation are specific DNA constructs known as nanostars, where the maximum number of bonds that each particle can create can be controlled by design. A nanostar of valence \mathcal{V} is formed by \mathcal{V} single DNA strands hybridised together and capable of binding to each other through sticky ends [2, 11]; control on the system bonding modes is achieved through the selection of the base sequences making up the nanostar binding sites, so that only specific sticky ends can bind to each other.

Given the complexity of the DNA molecule, formed by long chains of nucleotides containing dozens of atoms, any atomistic descriptive model is unsuitable to characterize its thermodynamic properties: the high number of degrees of freedom would make the simulations extremely large and therefore unmanageable in terms of implementation and timing [14]. One possibility to simplify the problem consists in using particle-based coarse-grained models [15], which indeed makes it possible to access the timescales required to study collective phenomena [16, 17]. However, phenomena such as phase separation and coarsening are still out of reach at such a level of description.

Here we tackle the problem by using a different approach based on the Cahn-Hilliard equation [18], which is a phase-field, partial differential equation describing the time evolution of the macroscopic order parameter density ρ , initially developed for the study of metal alloys, but in general suitable for the description of fluid mixtures with one or more components [18, 19]. Differently from previous attempts [20], based on schematic free-energy expressions, we describe the thermodynamics of the DNA nanostar systems in a realistic way making use of a mean-field free energy which has been developed to model self-assembling systems, and has been shown to qualitatively predict the properties of these DNA constructs [2].

Our aim is to assess the validity and potential of this *phase-field* model, as well as its predictive accuracy with respect to theoretical expectations and especially experimental results: the latter match is of particular interest because of the wide range of potential applications in biophysics involving nanostar-based systems, which include the possibility to mimic the liquid-liquid phase separation processes that are important for many cellular processes [21]. In this regard, an interesting analysis was carried out by Saleh et al. in [22], where a system of two different kinds of nanostars with interspecies linkers was studied experimentally, highlighting physical trends (especially in connection with interspecies surface tension variations with the concentration of cross-linkers) which we reproduce here.

II. METHODS

1. Cahn-Hilliard equation

The Cahn-Hilliard (CH) equation is a partial differential equation, derived from the assumption that the total free energy of a homogeneous system described by the number densities ρ_i of the N_s components at volume V and temperature T can be approximated as [18]

$$F(T, V) = \int_V \left[f(\{\rho_i\}) + \frac{K}{2} \sum_{i=1}^{N_s} (\vec{\nabla} \rho_i)^2 \right] dV, \quad (1)$$

where $f(\{\rho_i\})$ is the Helmholtz free-energy density, $\{\rho_i\}$ is the set of order parameters relevant to the system, and K is a coefficient linked to the free energy penalty that comes with the creation of an interface between two phases. To simplify the model, we neglect cross-species interfacial terms and we implicitly set K to be the same for all species.

By connecting the spatial variation of the order parameters with the spatial variation of a “generalised” chemical potential, it is possible to obtain a continuity equation that expresses locally the conservation of the total mass of the system [18]:

$$\frac{\partial \rho_j}{\partial t} = M \nabla^2 \left(\frac{\partial f(\{\rho_i\})}{\partial \rho_j} - K \nabla^2 \rho_j \right). \quad (2)$$

In Eq. (2) t is the time, M is a positive mobility coefficient setting the time scale of the system which we assume to be density-independent, ∇^2 is the spatial Laplacian operator, and the terms in brackets correspond to the generalised chemical potential of species j , $\mu_j = \partial f(\{\rho_i\})/\partial \rho_j - K \nabla^2 \rho_j$. This is the CH equation for the j -th number density which, given initial conditions and appropriate boundary conditions, can be numerically integrated in time to obtain the evolution of the system.

We discretise Eq. 2 in time with time step Δt , and in space by using bins of linear size Δx . We consider periodic boundary conditions. In order to integrate Eq. (3) in time we have implemented one explicit and two semi-implicit methods. Indeed, in addition to the explicit Euler method, which we have used throughout the paper, we have also implemented the implicit-explicit Euler method [23], which is solved in Fourier space, and the finite-volume scheme of Bailo *et al.* [24], discussed in Appendix A. We perform simulations in one- and two-dimensions using a parallel code that runs on GPUs to improve performance [25]. In our implementation, we use dimensionless free energies, multiplying their expressions by $\beta = \frac{1}{k_B T}$ for convenience. As a result, we use a rescaled mobility coefficient $M' = k_B T M$, which we set to a constant value $M' = 1$ (nm s) $^{-1}$, since its value affects the speed of the computations, but not the final configuration features. Therefore, in our implementation the equation we integrate becomes

$$\frac{\partial \rho_j}{\partial t} = M' \nabla^2 \left(\frac{\partial \beta f(\{\rho_i\})}{\partial \rho_j} - \beta K \nabla^2 \rho_j \right). \quad (3)$$

Additional details on the numerical methods, and in particular on the integration algorithm, can be found in Appendix A.

2. Wertheim free energy

The physics of the system is contained in the expression for the free energy density $f(\{\rho_i\})$, which has to be chosen carefully in order to reproduce with satisfactory accuracy the properties of the target system. For this purpose we use Wertheim theory [26, 27] for self-assembly, suitably adapted to a system of DNA nanostars in a $NaCl$ solution at fixed temperature T and salt concentration $[Na^+]$.

In the Wertheim theory, the free energy is written as a sum of two terms [2]:

$$f(\{\rho_i\}) = f_{\text{ref}}(\{\rho_i\}) + f_{\text{bond}}(\{\rho_i\}), \quad (4)$$

where $f_{\text{ref}}(\{\rho_i\})$ is the free energy of a system where no bonding is possible, and therefore accounts for the purely

repulsive forces (mainly excluded volume and electrostatic effects acting between the negatively charged backbones of DNA strands), and $f_{\text{bond}}(\{\rho_i\})$ is an attractive contribution, discussed later on, stemming from the hybridisation between the complementary sticky ends of the nanostars.

Since we consider rather dilute systems, we approximate the reference free energy with a second-order virial expansion, as proposed in Ref. [2], giving:

$$\beta f_{\text{ref}} = \rho \log(v_0 \rho) - \rho + B_2 \rho^2 + \sum_{j=1}^{N_s} \rho_j \log\left(\frac{\rho_j}{\rho}\right), \quad (5)$$

where $\rho = \sum_j^{N_s} \rho_j$ is the total number density, N_s is the number of species, B_2 is the second-order virial coefficient of the nanostars (with a non-bonding sticky sequence), which has the dimensions of a volume, and v_0 is the inverse of the partition function of a single nanostar multiplied by the volume of the system [28]; the latter can be assumed to be independent of density, so that its value does not affect the phase equilibrium. In the above expression we assume that the value of B_2 is the same for all pairs of species of interacting nanostars, which is an accurate approximation since the nanostars we consider have the same geometry, differing only in the sequence of the sticky ends. In the following we set $B_2 = 2190 \text{ nm}^3$, a value that has been computed in Ref. [2] through two-body coarse-grained simulations and was shown to be weakly dependent on T for the salt concentration we will be using (0.5 M).

The attractive part $f_b(\{\rho_i\})$, described in detail below, takes into account the contribution due to the self-assembly of the nanostars.

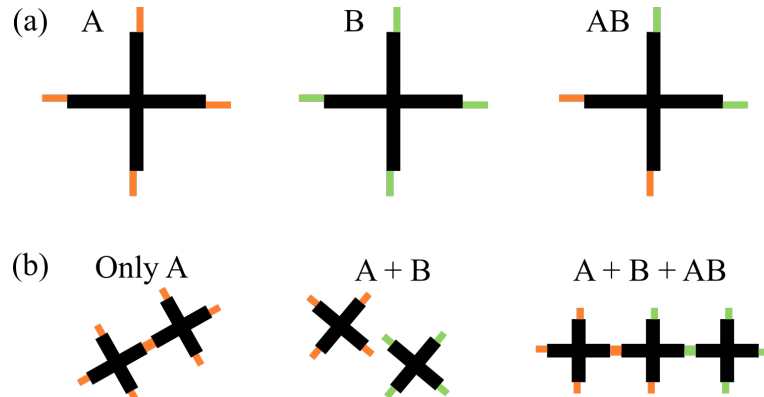


FIG. 1: A sketch representing (a) the different species of DNA nanostars we consider and (b) the way they can bond: only like-colour sticky ends can bind to each other. Each nanostar is composed by $\mathcal{V} = 4$ hybridised single strands of DNA (the black sections), each terminating with a single-stranded, self-complementary sticky sequence for connection with other nanostars (the coloured sections). Note that "only A" and "only B" systems have the same qualitative behaviour, while the presence of AB nanostars creates links between the A and the B particles.

As an example of a phase-field description of DNA-particle in solution we focus on the experimental system investigated by Saleh et al [22], which introduced three different nanostars, A , B and AB , with valence $\mathcal{V}_A = \mathcal{V}_B = \mathcal{V}_{AB} = \mathcal{V} = 4$. The two species of nanostars A and B have respectively four α and β orthogonal (*i.e.* non-complementary) palindromic sticky ends each, and are combined with special cross-linker AB nanostars for interspecies bonding. These cross-linkers are designed in such a way so as to contain two sticky ends of type α and two sticky ends of type β , thus promoting connections between the pure A and pure B species. In the presence of the AB nanostars, the A particles can bind among themselves and with the AB ones, and similarly the B particles can bind among themselves and with the AB ones, thus generating connections between the A and the B particles via the AB ones. For a graphical description of the bonding scheme, see Figure 1.

In the following we consider systems made of only A nanostars, as well as the Saleh et al [22] ternary mixtures of A , B , and AB . In the former case, the Wertheim bonding free-energy density is given by [2]

$$\beta f_b = \rho_A \mathcal{V} \left(\log(X_\alpha) + \frac{1 - X_\alpha}{2} \right) \quad (6)$$

where $X_\alpha(T, \rho_A, [Na^+]) = \frac{-1 + \sqrt{1 + 4\Delta_\alpha \mathcal{V} \rho_A}}{2\Delta_\alpha \mathcal{V} \rho_A}$ is the fraction of unbonded sticky ends at temperature T , salt concentration

$[Na^+]$, and density ρ_A , and Δ_α has the dimensions of a volume and quantifies the strength of the interaction acting between the specific complementary sequences of the sticky ends and is equal to:

$$\Delta_\alpha(T, [Na^+]) = v_b e^{-\beta \Delta G_\alpha} = v_b e^{-\beta(\Delta H_\alpha - T \Delta S_\alpha)}, \quad (7)$$

where $v_b = 1.66 \text{ nm}^3$ is the standard bonding volume associated with each particle, while ΔG_α is the Gibbs free energy variation associated with the hybridisation of two sticky ends α . The latter variation consists of two contributions, an enthalpic term, ΔH_α , and an entropic term, $\Delta S_\alpha = \Delta S^{\text{salt}} + \Delta S_\alpha^{\text{no salt}}$. The values of these two terms can be worked out from the specific sticky-end sequences of DNA bases using SantaLucia model [29, 30]. Table I contains the sequences (taken from [22]) and free-energy parameters of the sticky ends used in this work. Note that the chosen sequences are *palindromic* (i.e. self-complementary) to allow for $\alpha\alpha$ and $\beta\beta$ bonding, and that we fix the value of the salt concentration $[Na^+] = 0.5 \text{ M}$ throughout the whole paper.

In order to compare with numerical results, we use the one-component Wertheim free energy to calculate the phase diagram. The densities of the coexisting phases are found by using the Maxwell construction at fixed temperature [2].

Sticky sequences and descriptive parameters				
Sticky end	Sequence	$\Delta H \left[\frac{\text{cal}}{\text{mol}} \right]$	$\Delta S_{\text{salt}} \left[\frac{\text{cal}}{\text{mol K}} \right]$	$\Delta S_{\text{nosalt}} \left[\frac{\text{cal}}{\text{mol K}} \right]$
α	CGATCG	-42200	$1.84 \log([Na^+])$	-119.1
β	GAGCTC	-42400	$1.84 \log([Na^+])$	-120.6

TABLE I: Nucleotide sequences for the two kinds of sticky ends considered in this study, and enthalpic and entropic variations associated with their hybridisation calculated according to Ref. [29, 30].

With the free energy contributions given in Eqs. 5 and 6, the Cahn-Hilliard equation can be written explicitly for this pure system, giving:

$$\frac{\partial \rho_A}{\partial t} = M' \nabla^2 (\beta \mu_{\text{ref}} + \beta \mu_b + \beta \mu_{\text{int}}) \quad (8)$$

in which the chemical potential contributions from the reference, bonding and interface terms come respectively in the form $\beta \mu_{\text{ref}}(\rho_A) = \frac{df_{\text{ref}}(\rho_A)}{d\rho_A} = \log(\rho_A) + 2B_2 \rho_A$, $\beta \mu_b(\rho_A) = \frac{df_b(\rho_A)}{d\rho_A} = \mathcal{V} \log(X_\alpha(T, \rho_A))$ and $\mu_{\text{int}}(\nabla \rho_A) = -K \nabla^2 \rho_A$.

For Saleh's mixture, the attractive contribution f_b takes the following form [2]:

$$\beta f_b = \rho_A \mathcal{V} \left(\log(X_\alpha) - \frac{X_\alpha}{2} + \frac{1}{2} \right) + \rho_B \mathcal{V} \left(\log(X_\beta) - \frac{X_\beta}{2} + \frac{1}{2} \right) + \rho_{AB} \frac{\mathcal{V}}{2} \left(\log(X_\beta) - \frac{X_\beta}{2} + \log(X_\alpha) - \frac{X_\alpha}{2} + 1 \right) \quad (9)$$

where X_α and X_β correspond to the fraction of unbonded sticky ends of type α and β , respectively, and are given by:

$$X_\gamma = \frac{-1 + \sqrt{1 + 4c_\gamma \Delta_\gamma}}{2c_\gamma \Delta_\gamma}, \quad (10)$$

where $\gamma \in \{\alpha, \beta\}$ and c_γ is the number density of sticky ends of type γ , i.e. $c_\alpha = \mathcal{V}(\rho_A + \frac{\rho_{AB}}{2})$ and $c_\beta = \mathcal{V}(\rho_B + \frac{\rho_{AB}}{2})$.

Finally, the system of coupled differential equations to be solved to obtain the time evolution dynamics of the three density fields can be written as:

$$\frac{\partial \rho_i}{\partial t} = M' \nabla^2 (\beta \mu_{\text{ref}}^i + \beta \mu_b^i + \beta \mu_{\text{int}}^i) \quad i \in \{A, B, AB\}$$

where the chemical potential contributions for species i amount to $\beta \mu_{\text{ref}}^i(\rho_i, \rho) = 2B_2 \rho + \log \rho_i$, $\beta \mu_b^i(\{\rho_j\}) = \sum_{\gamma \in \Gamma(i)} \log X_\gamma$ and $\mu_{\text{int}}^i(\nabla \rho_i) = -K \nabla^2 \rho_i$. Here $\Gamma(i)$ refers to the set of sticky ends present on nanostars of type i , and K is the interfacial cost, which we assume independent of i .

III. RESULTS

A. Pure systems

We use the one-component system made by A nanostars to assess the effectiveness and reliability of the present Cahn-Hilliard based approach, as well as to select an optimal value for the βK constant.

It was shown experimentally that, under the right thermal and density conditions the only- A system phase separates into a high-density phase containing a network of bonded nanostars (the liquid), and a low-density phase composed of mostly unbonded nanostars (the gas) [11]. Within the present approach, we also find that any initial configuration defined by small random density fluctuations superimposed to an average value evolves according to the CH equations or toward a completely homogeneous system, or toward a phase-separated system, as shown in Figure 2 for a 2D system.

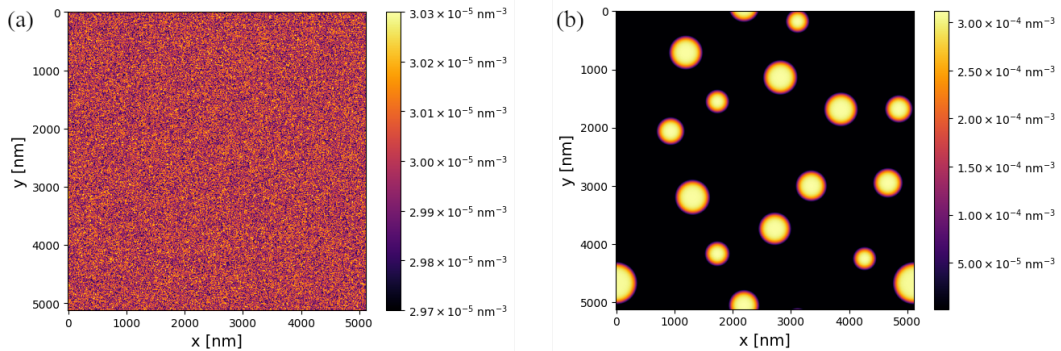


FIG. 2: Initial and final configurations of a simulation of a one-component A system at $T = 303.15$ K. (a) Initially the system is initialised in a quasi-homogeneous configuration, where each bin has a nanostar number density close to $\rho_A = 3 \times 10^{-5} \text{ nm}^{-3}$. (b) After $\approx 10^8$ steps run with $\Delta t = 10^{-5}$ s, the system is well separated, with liquid droplets coexisting with a gas background.

The coefficient K appearing in the Cahn-Hilliard equation is associated to the Helmholtz free energy cost associated with the creation of an interface between two different phases. Indeed, the free energy penalty for interface creation comes in the form $\frac{K}{2} |\nabla \rho|^2$, which means that for a given interface cost, increasing the value of K decreases the density gradient magnitude $|\nabla \rho|$, thus making the interface smoother and wider. Of course, decreasing K does the opposite.

Here we set the value of βK by comparing the theoretical gas-liquid phase diagram, obtained by using the Maxwell construction with the free energy given by Eq. (4), with numerical results of 1D Cahn-Hilliard simulations. We fix the timestep, $\Delta t = 10^{-6}$ s, and the grid spacing $\Delta x = 10$ nm, and run simulations at four different temperatures, $T = 298.15, 303.15, 308.15$ and 309.15 K, for 10^{10} time steps. Note that the highest T is just above the theoretical critical temperature, and therefore does not phase separate. For each state point we use three values of the interface constant, $\beta K = 10^5, 10^6$ and 10^7 nm^5 , and two different initial conditions: *separated* and *homogeneous*. The former refers to a starting configuration where the two halves of the system are initialised with the theoretical densities of the gas and the liquid, ρ_g and ρ_l , connected by sigmoidal curves. By contrast, in *homogeneous* simulations we start with a system of average density $(\rho_g + \rho_l)/2$, with random fluctuations around this value.

Figure 3(a) shows the comparison between theory and simulation. First of all, we note that all simulations predict the homogeneity at the highest temperature considered, in agreement with theory. Secondly, below the critical temperature T_c , the densities of the two coexisting phases are well-reproduced by the simulations, with two exceptions. For $T = 308.15$ K, which is just below T_c , the $\beta K = 10^7 \text{ nm}^5$ coexisting densities are closer than what they should be. We identify this disagreement as a finite-size effect, as at this temperature and value of βK the width of the interface becomes comparable with the box size. By contrast, if $\beta K = 10^5 \text{ nm}^5$, low-temperature simulations started from homogeneous configurations tend to underestimate the liquid density. This happens because the dynamics slows down massively, as seen by the much smaller values of the time derivative of the density field for the $\beta K = 10^5 \text{ nm}^5$ system (not shown), which therefore remains stuck in a metastable configuration. The final density profiles of systems displaying these two effects are shown in Fig. 3(b) and compared to density profiles of systems with $\beta K = 10^6 \text{ nm}^5$, which achieve the correct liquid density at the end of the simulation.

These results show that setting $\beta K = 10^6 \text{ nm}^5$ provides, for the system size studied in this study, correct estimates of the equilibrium densities and that equilibration takes place in reasonable computational times for the explored range of temperatures. Thus we decided to fix βK to this value for the rest of this work.

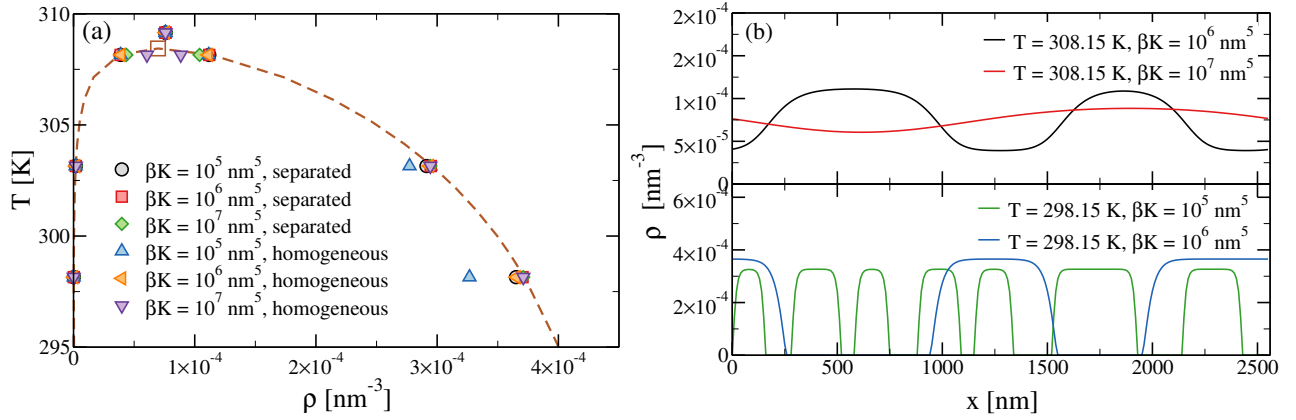


FIG. 3: (a) A comparison between the theoretical (brown dashed lines) and numerical (filled symbols) phase diagrams, for three values of βK and two different initial conditions. The brown open square signals the position of the critical point. (b) Final density profiles for simulations run at (top) $T = 308.15 \text{ K}$ and (bottom) $T = 298.15 \text{ K}$, for two different values of the interfacial cost βK .

We also estimate the surface tension γ associated to the gas-liquid interface, which is defined as the free-energy cost per unit area of forming the interface. Since we have access to the total free energy of a system through Eq. (1), we can directly estimate γ by using its definition. In order to do so, we evaluate the free energy of two systems initialised with the coexisting densities of either the gas or the liquid phase, yielding F_{gas} and F_{liquid} . We then put these two systems in contact and simulate the formation of two interfaces (through periodic-boundary conditions) of interface area A . At long times, the free energy of the system converges to a value F_{coex} . The surface tension can then be estimated as

$$\gamma = \frac{F_{\text{coex}} - (F_{\text{gas}} + F_{\text{liquid}})}{2A}, \quad (11)$$

In 1D we use systems made of $N = 128$ bins, and $A = \Delta x^2$, since the system can be thought of as a parallelepiped of physical dimensions $N\Delta x \times \Delta x \times \Delta x$. By contrast, in 2D $A = N\Delta x^2$, since the size of the simulation box is $N\Delta x \times N\Delta x \times \Delta x$.

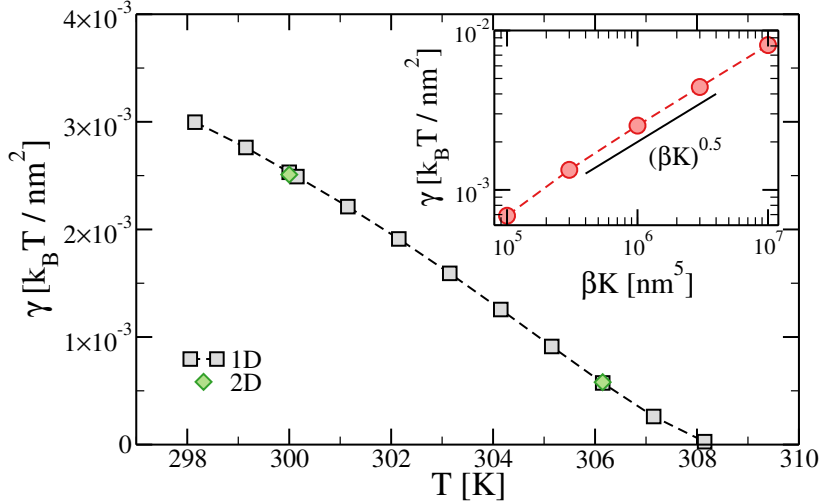


FIG. 4: The surface tension of the one-component A system, γ , as a function of temperature. The black and green symbols refer to 1D and 2D systems, respectively. Inset: γ as a function of βK for $T = 300 \text{ K}$. The observed dependency is compatible with a square root.

Close to the critical point, the surface tension scales as $\gamma \propto \left(\frac{T_c - T}{T_c}\right)^\mu$, where μ is a critical exponent that depends

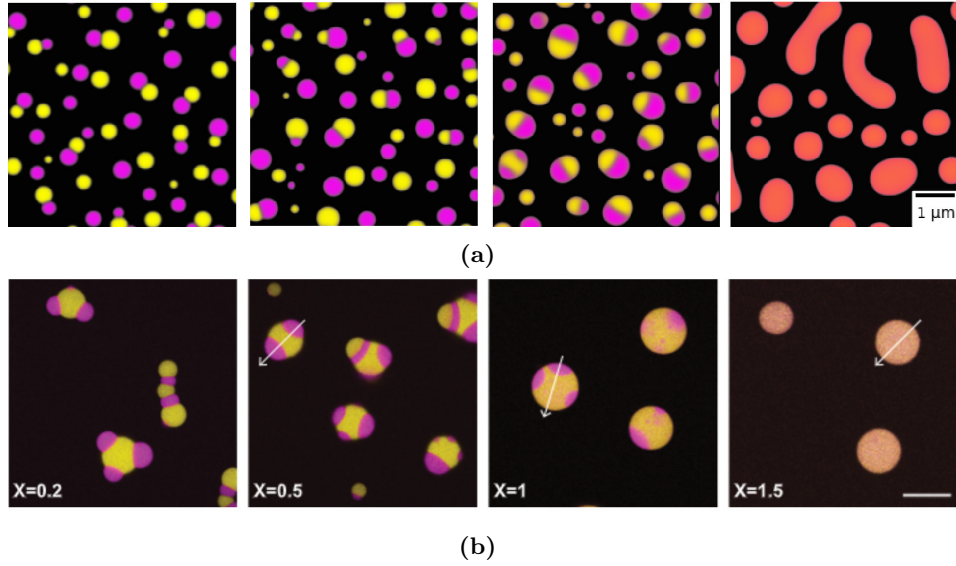


FIG. 5: (a) Simulated configurations of phase-separated systems as the cross-linker fraction c_X is increased, from left to right. Each pixel is coloured according to the density of each species it contains, where species A and B are associated to magenta and yellow, respectively. The simulations have been run at $T = 300$ K and average densities $\rho_A = \rho_B = 2 \times 10^{-5} \text{ nm}^{-3}$ and $\rho_{AB} = c_X \rho_A$, with $c_X \in \{0.2, 0.5, 1.0, 1.5\}$. The scale bar corresponds to $1 \mu\text{m}$. (b) Experimental configurations of phase-separated systems corresponding to increasingly higher (from left to right) values of $c_X \in \{0.2, 0.5, 1.0, 1.5\}$, taken at $T = 293.15$ K and $\rho_A = \rho_B = 3.0 \times 10^{-6} \text{ nm}^{-3}$. Species A and B are tagged with two different fluorescent molecules: magenta and yellow, respectively. The scale bar corresponds to $20 \mu\text{m}$. Adapted with permission from [22].

on the universality class of the system. As shown in Figure 4, we find that the surface tension decreases linearly with temperature, in agreement with the mean-field nature of Wertheim theory. Interestingly, sufficiently apart (1-2 K) from the critical point, $\gamma \sim 10^{-3} k_B T / \text{nm}^2$, which is compatible with experimental estimates of the surface tension of DNA nanostars [22, 31]. We also computed the surface tension for two 2D systems using the GPU code, and the results are fully compatible with the 1D CPU data. Finally, in the inset of Fig. 4 we show that $\gamma \propto \sqrt{K}$, as expected in CH simulations [32].

B. Three-component systems

We now move on to the computational study of the three-component system of Saleh *et al.*, who investigated the properties of phase separated systems for different values of the fraction of the AB cross-linkers $c_X = \frac{\rho_{AB}}{\rho_A}$. In the simulations for this part, we fix the temperature to $T = 300$ K (which is below the critical temperature T_c , otherwise the system would remain homogeneous according to Wertheim theory) and simulate grids made of 1024×1024 bins of width $\Delta x = 10$ nm. The selected temperature is slightly higher than the experimental one, $T = 293.15$ K. While this difference is not expecting to change the physics of the phase separation process, it allows us to follow the phase separation kinetics for longer times, helping the comparison with the experimental results. We also note that since Wertheim theory is known to reproduce the thermodynamics of DNA nanostars only in a semi-quantitative manner [2, 13, 33], it is not obvious that using the experimental temperature would result in a more precise comparison.

We focus on the effect of the cross-linkers by simulating systems with a fixed and equal density of A and B nanostars, *e.g.* $\rho_A = \rho_B$, to which we add a fraction $c_X \rho_A$ of cross-linkers. When c_X is zero or small, then both the A and the B nano-stars undergo a gas-liquid phase separation similar to the one-component case, where the A and B species form completely demixed liquid droplets. As c_X increases, the tendency of the cross-linkers to bond to both species lowers the $A - B$ liquid-liquid surface tension, leading to systems made of fused droplets, which are still partially demixed. For $c_X > 1$, the abundance of cross-linkers requires that A and B co-localise, resulting in liquid droplets where the A and B species are fully mixed. As shown in Figure 5a, the solutions of the CH equation for the chosen values of c_X display exactly this behaviour, in qualitative agreement with the experimental study results reproduced in Figure 5b [22], as well as with recent experiments on RNA-based condensates [34]. Note that the density of the

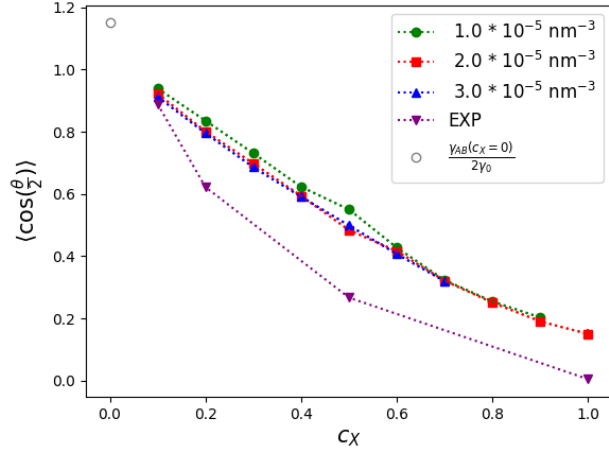


FIG. 6: Surface tension study as a function of cross-linker concentration c_X in comparison with experimental data. The theoretical estimates at $\rho_A = \rho_B = \{1.0 \times 10^{-5}, 2.0 \times 10^{-5}, 3.0 \times 10^{-5}\} \text{ nm}^{-3}$ have been obtained from averaging over $N = 4$ equilibrated configurations at each state point; the calculation of $\cos \theta$ for each binary cluster was automated exploiting Python libraries by fitting curves on each species contour and calculating derivatives at the contact points. The empty point $\frac{\gamma_{AB}(c_X=0)}{2\gamma_0}$ has been derived empirically by measuring $\gamma_{AB}(c_X = 0)$ similarly to γ , *i.e.* through total free energy subtraction methods. Note that in the figure error bars are smaller than symbol size.

numerical and experimental systems differ by almost an order of magnitude, owing to the different (smaller) time scales accessible with our method.

From the final simulation configurations we identify all the droplets formed by two fused pure-*A* and pure-*B* droplets, and then measure the contact angle θ formed at each junction between the gas, liquid *A* and liquid *B* phases. Exploiting the *von-Neumann* convention to express the *A*–*B* surface tension in terms of θ , and imposing mechanical equilibrium, the liquid-gas and *A*–*B* surface tensions, γ and γ_{AB} are connected by $\gamma_{AB} = 2\gamma \cos \frac{\theta}{2}$. In the experimental study, it was assumed that $\gamma_{AB}(c_X = 0) = 2\gamma$. Here we can independently estimate $\gamma_{AB}(c_X = 0)$ by using Eq. 11, with F_A and F_B , the total free energy of two pure *A* and *B* systems, in place of F_{gas} and F_{liquid} , respectively.

Figure 6 shows $\cos \frac{\theta}{2}$ as a function of c_X , for three different average densities of species *A* and *B*, with $\rho_A = \rho_B$. All curves display a decreasing trend for surface tension as the fraction of linkers c_X is increased, in agreement with theory; it is worth noticing that the average densities $\rho_A = \rho_B$ do not seem to significantly affect the plotted quantity, as suggested by the quasi-overlapping points obtained at different densities, although the low-density measurements marginally diverge from the others, which is likely due to the smaller size of clusters altering the contact angle. We note that the agreement between simulation and experiment is only semi-quantitative, as the numerical results are always higher than the experimental data, which falls off to zero for $c_X \approx 1$; this mismatch may be due to the assumptions behind the theory we use, to the significantly lower density $\rho_A = \rho_B = 3.0 \times 10^{-6} \text{ nm}^{-3}$ in which experiments were carried out, to the different temperature of the experiments (namely $T = 293.15 \text{ K}$), and to generally different and incomparable observation time scales. Unlike the experimental points, our simulation-extracted measurements also seems to describe a linear variation of $\langle \cos \frac{\theta}{2} \rangle$ with respect to c_X at low values of c_X .

IV. CONCLUSIONS

In conclusion, we have shown that the venerable Cahn-Hilliard equation can be used to study the kinetics of phase separation in DNA-based systems by leveraging an expression for the free energy that models the self-assembly process. We have shown that this approach can be generalised to mixtures of many molecular species, and that its theoretical consistency and qualitative agreement with experimental trends make it a powerful means of characterization for the properties of self-assembling systems. Indeed, the phase-field method introduced here offers the possibility of simulating larger time and length scales with respect to molecular descriptions.

Our study shows that the Wertheim theory [26, 27], associated to the CH equation provided an accurate description of available experimental data. Minor differences are still observed in the dependence of the contact angle on the

fraction of cross-linkers. It will be interesting to understand in depth the origin of these differences and if these are related to the simplifying choices adopted (for example the absence of thermal noise and the hypothesis of equal K for each component), or to other factors such as the different density in the experiments and in the simulations, or the different time covered in experiments and in our study.

There are few aspects that can be optimized to fully uncover the potential of this approach, including integrating thermal noise in the Cahn-Hilliard equation (as done, *e.g.*, in [20]) and potentially increasing the integration time-step through more refined numerical algorithms [24, 35].

We envision applications for this method in the context of multi-component liquid-liquid phase separation in cells [36, 37], to investigate the kinetics of self-assembly in complex geometries [38], or to model the coupling between thermodynamics and matter flow (*e.g.* by coupling the Cahn-Hilliard equation to Stokes or Navier-Stokes equations [39, 40]).

ACKNOWLEDGEMENTS

We thank Silvio Bianchi and Omar A. Saleh for useful discussions. We acknowledge support by ICSC – Centro Nazionale di Ricerca in High Performance Computing, Big Data and Quantum Computing, funded by European Union – NextGenerationEU, and CINECA-ISCRA for HPC resources.

Appendix A: Additional details on the numerical algorithm

In order to integrate Eq. (3) in time we have implemented one explicit and two semi-implicit methods. Indeed, in addition to the explicit Euler method, which we have used throughout the paper, we have also implemented the implicit-explicit Euler method [23], which is solved in Fourier space, and the finite-volume scheme of Bailo *et al.* [24]. The latter two have better properties when it comes to mass conservation and free-energy dissipation, which usually means that they make it possible to use smaller values of Δt . This is especially true for the scheme of Ref. [24], which is unconditionally stable. Unfortunately, it also requires to solve a system of non-linear equations at each time step, which dramatically decreases the overall performance and makes it essentially unusable, at least with our implementation, for systems with a number of bins N larger than a few hundred.

As for the explicit and implicit-explicit Euler methods, unfortunately, our tests showed that the logarithmic term of the ideal gas, which diverges as the density goes to zero, does not make it possible to exploit the improved stability of the latter. Common techniques such as logarithmic regularisation [41] did not help. As a result, in both schemes we have to rely on very small values of the integration time step. Moreover, the scaling of the Fourier scheme is bound by the performance of the Fast-Fourier Transform method, which is $\mathcal{O}(N \log N)$. Therefore, for the rather large number of bins we use for the 2D simulations, where $N \approx 10^6$, the simpler explicit Euler scheme, whose performance scales as $\mathcal{O}(N)$, yields a four-fold speed-up and no sensibly worse quality of the results. The code we used to run the simulations is freely available online [25].

[1] A. Travers and G. Muskhelishvili, Dna structure and function, *The FEBS Journal* **282** (2015).

[2] E. Locatelli, P. H. Handle, C. N. Likos, F. Sciortino, and L. Rovigatti, Condensation and demixing in solutions of dna nanostars and their mixtures, *ACS Nano* **11** (2017).

[3] A. Wollman, C. Sanchez-Cano, H. Carstairs, R. Cross, and A. Tuberfield, Transport and self-organization across different length scales powered by motor proteins and programmed by dna, *Nat. Nanotechnology* **9** (2013).

[4] D. Soloveichik, G. Seelig, and E. Winfree, Dna as a universal substrate for chemical kinetics, *Proc. Natl. Acad. Sci. U.S.A.* **107** (2010).

[5] P. Rothemund, Folding dna to create nanoscale shapes and patterns, *Nature* **440** (2006).

[6] Y.-X. Zhao, A. Shaw, X. Zeng, E. Benson, A. Nystrom, and B. Hogberg, Dna origami delivery system for cancer therapy with tunable release properties, *ACS Nano* **6** (2012).

[7] Y. Ke, L. L. Ong, W. M. Shih, and P. Yin, Three-dimensional structures self-assembled from dna bricks, *Science* **338** (2012).

[8] A. Reinhardt and D. Frenkel, Dna brick self-assembly with an off-lattice potential, *Soft Matter* **12** (2016).

[9] Q. Hu, H. Li, L. Wang, H. Gu, and C. Fan, Dna nanotechnology-enabled drug delivery systems, *Chem. Rev.* **119** (2019).

[10] E. Bianchi, J. Largo, P. Tartaglia, E. Zaccarelli, and F. Sciortino, Phase diagram of patchy colloids: Towards empty liquids, *Phys. Rev. Lett.* **97** (2006).

[11] S. Biffi, R. Cerbino, F. Bomboi, E. M. Paraboschi, R. Asselta, F. Sciortino, and T. Bellini, Phase behavior and critical activated dynamics of limited-valence dna nanostars, *Proceedings of the National Academy of Sciences* **110** (2013).

- [12] N. Conrad, T. Kennedy, D. K. Fygenson, and O. A. Saleh, Increasing valence pushes dna nanostar networks to the isostatic point, *Proceedings of the National Academy of Sciences* **116**, 7238 (2019).
- [13] N. Conrad, G. Chang, D. K. Fygenson, and O. A. Saleh, Emulsion imaging of a dna nanostar condensate phase diagram reveals valence and electrostatic effects, *The Journal of Chemical Physics* **157** (2022).
- [14] T. Sun, A. Mirzoev, V. Minhas, N. Korolev, A. P. Lyubartsev, and L. Nordenskiöld, A multiscale analysis of dna phase separation: from atomistic to mesoscale level, *Nucleic Acids Res.* **47** (2019).
- [15] J. J. de Pablo, Coarse-grained simulations of macromolecules: From dna to nanocomposites, *Annu. Rev. Phys. Chem.* **62** (2011).
- [16] P. Šulc, F. Romano, T. E. Ouldridge, L. Rovigatti, J. P. K. Doye, and A. A. Louis, Sequence-dependent thermodynamics of a coarse-grained dna model, *The Journal of Chemical Physics* (2012).
- [17] E. Poppleton, M. Matthies, D. Mandal, F. Romano, P. Šulc, and L. Rovigatti, The oxdna coarse-grained model as a tool to simulate dna origami, *Methods in Molecular Biology* (2023).
- [18] H. Wu, A review on the cahn–hilliard equation: classical results and recent advances in dynamic boundary conditions, *Electronic Research Archive* **30** (2022).
- [19] R. Abazari, H. Rezazadeh, L. Akinyemi, and M. Inc, Numerical simulation of a binary alloy of 2d cahn–hilliard model for phase separation, *Computational and Applied Mathematics* **41** (2022).
- [20] S. Wilken, A. Chaderjian, and O. A. Saleh, Spatial organization of phase-separated dna droplets, *Physical Review X* **13** (2023).
- [21] S. F. Banani, H. O. Lee, A. A. Hyman, and M. K. Rosen, Biomolecular condensates: organizers of cellular biochemistry, *Nature reviews. Molecular cell biology* **18**, 285–298 (2017).
- [22] B. Jin Jeon, D. T. Nguyen, and O. A. Saleh, Sequence-controlled adhesion and microemulsification in a two-phase system of dna liquid droplets, *Journal of Physical Chemistry* **124** (2020).
- [23] E. d. A. Soares, A. G. Barreto Jr, and F. W. Tavares, Exponential integrators for phase-field equations using pseudo-spectral methods: A python implementation, *arXiv preprint arXiv:2305.08998* (2023).
- [24] R. Bailo, J. A. Carrillo, S. Kalliadasis, and S. P. Perez, Unconditional bound-preserving and energy-dissipating finite-volume schemes for the cahn-hilliard equation, *Communications in Computational Physics* **34** (2023).
- [25] M. Cappa and L. Rovigatti, lorenzo-rovigatti/: v1.0.0, 10.5281/zenodo.14576360 (2024).
- [26] M. S. Wertheim, Fluids with highly directional attractive forces. i. statistical thermodynamics, *Journal of statistical physics* **35**, 19 (1984).
- [27] M. S. Wertheim, Fluids with highly directional attractive forces. iii. multiple attraction sites, *Journal of statistical physics* **42**, 459 (1986).
- [28] D. A. McQuarrie, *Statistical Mechanics* (2000).
- [29] J. SantaLucia, A unified view of polymer, dumbbell, and oligonucleotide dna nearest-neighbor thermodynamics, *Proceedings of the National Academy of Sciences* **95** (1998).
- [30] J. SantaLucia and D. Hicks, The thermodynamics of dna structural motifs, *Annual Review of Biophysics and Biomolecular Structure* **33** (2004).
- [31] B.-j. Jeon, D. T. Nguyen, G. R. Abraham, N. Conrad, D. K. Fygenson, and O. A. Saleh, Salt-dependent properties of a coacervate-like, self-assembled dna liquid, *Soft Matter* **14**, 7009 (2018).
- [32] J. W. Cahn and J. E. Hilliard, Free energy of a nonuniform system. i. interfacial free energy, *The Journal of chemical physics* **28**, 258 (1958).
- [33] E. Locatelli and L. Rovigatti, An accurate estimate of the free energy and phase diagram of all-dna bulk fluids, *Polymers* **10**, 447 (2018).
- [34] G. Fabrini, N. Farag, S. P. Nuccio, S. Li, J. M. Stewart, A. A. Tang, R. McCoy, R. M. Owens, P. W. Rothemund, E. Franco, *et al.*, Co-transcriptional production of programmable rna condensates and synthetic organelles, *Nature Nanotechnology* , 1 (2024).
- [35] X. Yang and G.-D. Zhang, Convergence analysis for the invariant energy quadratization (ieq) schemes for solving the cahn–hilliard and allen-cahn equations with general nonlinear potential, *Journal of Scientific Computing* **82** (2020).
- [36] S. F. Banani, A. M. Rice, W. B. Peebles, Y. Lin, S. Jain, R. Parker, and M. K. Rosen, Compositional control of phase-separated cellular bodies, *Cell* **166**, 651 (2016).
- [37] J. A. Riback, L. Zhu, M. C. Ferrolino, M. Tolbert, D. M. Mitrea, D. W. Sanders, M.-T. Wei, R. W. Kriwacki, and C. P. Brangwynne, Composition-dependent thermodynamics of intracellular phase separation, *Nature* **581**, 209 (2020).
- [38] Y. Li, J.-I. Choi, and J. Kim, Multi-component cahn–hilliard system with different boundary conditions in complex domains, *Journal of Computational Physics* **323**, 1 (2016).
- [39] J. Kim and J. Lowengrub, Phase field modeling and simulation of three-phase flows, *Interfaces and free boundaries* **7**, 435 (2005).
- [40] F. Boyer, C. Lapuerta, S. Minjeaud, B. Piar, and M. Quintard, Cahn–hilliard/navier–stokes model for the simulation of three-phase flows, *Transport in Porous Media* **82**, 463 (2010).
- [41] D. Li and T. Tang, Stability of the semi-implicit method for the cahn-hilliard equation with logarithmic potentials, *Ann. Appl. Math.* **37**, 31 (2021).